

Emergent charge order from correlated electron-phonon physics in cuprates

Saikat Banerjee, W. A. Atkinson, Arno P. Kampf

Angaben zur Veröffentlichung / Publication details:

Banerjee, Saikat, W. A. Atkinson, and Arno P. Kampf. 2020. "Emergent charge order from correlated electron-phonon physics in cuprates." *Communications Physics* 3 (1): 161. <https://doi.org/10.1038/s42005-020-00430-1>.

Emergent charge order from correlated electron-phonon physics in cuprates

S. Banerjee ¹✉, W. A. Atkinson ² & A. P. Kampf¹

Charge-density wave order is now understood to be a widespread feature of underdoped cuprate high-temperature superconductors, although its origins remain unclear. While experiments suggest that the charge-ordering wavevector is determined by Fermi-surface nesting, the relevant sections of the Fermi surface are featureless and provide no clue as to the underlying mechanism. Here, focusing on underdoped $\text{YBa}_2\text{Cu}_3\text{O}_{6+x}$, we propose that charge-density waves form from the incipient softening of a bond-buckling phonon. The momentum dependence of its coupling to itinerant electrons favourably selects the wavevector found in experiments. But, it requires quasiparticle renormalization by strong electronic correlations to enable a unique enhancement of the charge susceptibility near the B_{1g} -phonon selected wavevector. The B_{1g} phonon frequency softens by a few percent, and finite-range charge-density wave correlations will form locally, if nucleated by defects or dopant disorder. These results suggest that underdoped cuprates cannot be understood in the context of strong electronic correlations alone.

¹Theoretical Physics III, Center for Electronic Correlations and Magnetism, Institute of Physics, University of Augsburg, Augsburg 86135, Germany.

²Department of Physics and Astronomy, Trent University, Peterborough, Ontario K9L 0G2, Canada. ✉email: saikat.banerjee@physik.uni-augsburg.de

The discovery of charge-density wave (CDW) order¹ in underdoped cuprates raised the question of whether it is intimately related to pseudogap physics^{2–7}, and thereby yet another signature of strong electronic correlations. Charge modulations with a moderate correlation length are detected by nuclear magnetic resonance^{8–10}, scanning tunneling microscopy (STM)^{11–13}, and X-ray techniques^{11,12,14–16}, with the latter finding incommensurate wave-vectors near $\mathbf{q}_{\text{CO}} = 0.3$ reciprocal lattice units, oriented along the crystalline axes with either uniaxial or biaxial character. The CDW wavevector \mathbf{q}_{CO} continuously drops with increasing hole doping in $\text{YBa}_2\text{Cu}_3\text{O}_{6+x}$ (YBCO) and $\text{Bi}_2\text{Sr}_{2-x}\text{La}_x\text{CuO}_{6+x}$ (Bi-2201)^{1,11,16,17}, whereas the completely opposite trend is observed in charge-stripe ordered La-based 214 cuprates such as $\text{La}_{2-x}\text{Sr}_x\text{CuO}_4$ (LSCO) and $\text{La}_{2-x}\text{Ba}_x\text{CuO}_4$ (LBCO)¹⁸. Also the concomitant spin-stripe order marks 214 cuprates to be different from YBCO or Bi-2201. Due to these apparent differences we focus on the charge ordering in YBCO.

Stripe formation and competition with d-wave superconductivity or pair-density waves was investigated for multiband Hubbard or t - J models with accurate computational tools^{19–21}. Charge-stripe ground states were found with a near-degeneracy of competing states. So far, the axial orientation and the incommensurate character of \mathbf{q}_{CO} , as well as its doping variation in YBCO and Bi-2201, proved difficult to reconcile with purely electronic model calculations^{20,22}. Weak-coupling theories typically predict that \mathbf{q}_{CO} lies on the Brillouin zone (BZ) diagonal^{5,23,24} unless the CDW instability is preceded by a Fermi surface reconstruction to form hole pockets⁷. Based on this evidence, we conjecture that some missing ingredient may still be required to explain charge-order in YBCO and Bi-2201.

In the continuing search for this ingredient, we employ further experimental facts. First, the discovery of charge order in overdoped Bi-2201, with an unreconstructed Fermi surface²⁵, poses a question as to whether the CDW is actually tied to the pseudogap phenomena. Second, the softening or broadening of phonon modes at the CDW wavevector^{26,27} along with giant phonon anomalies near the CDW instability, all point to a strong electron-phonon (el - ph) coupling²⁸. While the phonon dispersion will necessarily react to a charge-density modulation, phonons may also play a key role in CDW formation, for example selecting the ordering wavevector in CDW-susceptible materials^{29,30}. In cuprates, the frequencies of the phonons decrease only weakly, and a continuous softening to zero frequency is likely precluded by quenched disorder^{10,31}.

A third hint comes from the atomic displacement pattern that accompanies the CDW. A complete set of X-ray diffraction data, by Forgan et al.³², found the by-far largest displacements for planar oxygen atoms; they shift out-of-plane with an out-of-phase pattern (see Fig. 1) that closely resembles the normal mode of the B_{1g} bond-buckling phonon³³. In stoichiometric, overdoped YBCO the dispersion of the B_{1g} phonon was monitored upon cooling²⁶; even though the stoichiometric composition of YBCO

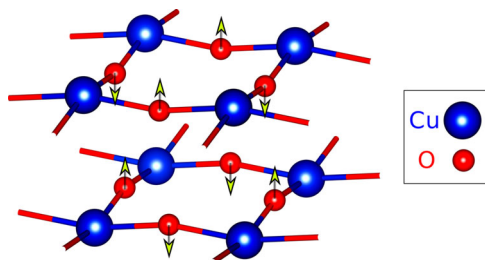


Fig. 1 Oxygen vibrations with B_{1g} symmetry. A representation of the out-of-plane oxygen vibrations (B_{1g} pattern) in a copper-oxide bilayer. The arrows represent the out-of-phase motions of the oxygen atoms.

does not support CDW order, the B_{1g} phonon frequency softens by about 6% at the charge ordering wavevector for underdoped YBCO. The X-ray diffraction data in Forgan et al.³² reveal that also the heavier ions in YBCO slightly move away from the positions they take in the charge homogeneous phase in equilibrium. This naturally suggests that also the low-energy phonons are involved in the CDW formation, and indeed the softening of a low-energy optical phonon was observed by Le Tacon et al.²⁸ and Kim et al.²⁷. While the softening of this mode indeed indicates a coupling to the CDW (as must occur in the absence of special symmetries), the small static displacements of the Ba and Y atoms observed in X-ray diffraction suggests ultimately that there is a relatively weak participation of this mode in the CDW formation.

There is, furthermore, a bond-stretching phonon that develops a Kohn-like anomaly as temperature is reduced^{34–41}. This temperature-dependent softening was initially understood to indicate strong el - ph coupling, and indeed the size of the anomaly correlates with the superconducting T_c ⁴⁰. However, trends with doping do not show any clear correlation with spin-charge stripes³⁹, static charge density waves⁴², or kinks in the electronic dispersion⁴⁰, which seems to rule out conventional el - ph coupling mechanisms of the type contemplated here. Rather, it is proposed that the softening reflects coupling to a collective charge mode of the electron liquid^{40,43}. In Forgan et al.³², oxygen displacements do indeed have in-plane components, indicating that the bond-stretching modes contribute alongside the buckling mode, but the out-of-plane components are dominant, and we make the simplifying approximation that the in-plane component can be neglected.

Based on these empirical grounds, we select the B_{1g} bond-buckling phonon, reanalyze its coupling to the electrons in the copper-oxygen planes, and obtain the Landau free energy for a B_{1g} -phonon mediated CDW. We start from a microscopic model for the CuO_2 planes, and find that the structure of the el - ph coupling matrix element $g(\mathbf{q}; \mathbf{k})$ depends strongly on the orbital content of the Fermi surface. In particular, the Cu-4s orbital is crucial; with it, $g(\mathbf{q}; \mathbf{k})$ is maximum at phonon momenta \mathbf{q}^* that are axial (rather than diagonal) and track the doping dependence of the CDW wavevector. The special role of \mathbf{q}^* is imperceptible in the free energy when calculated with bare electron dispersions.

Here, we show that with the inclusion of electronic correlations, modeled by a renormalization of the band dispersion and quasiparticle spectral weight, an axial wavevector close to \mathbf{q}^* emerges as the dominant wavevector in the CDW susceptibility. While the B_{1g} mode is, by itself, too weak (i.e., softens by only a few percent) to induce true long-range order, the inevitable presence of disorder will necessarily slow down and pin the CDW fluctuations, creating local patches of static or quasi-static charge order with finite correlation lengths. This leads us to propose a scenario, in which a phonon-based mechanism is enabled by strong electronic correlations, and the incommensurate wavevector of the concomitant charge correlations is dictated by the momentum-space structure of the el - ph coupling matrix element.

Results

Three-orbital electronic model. To set the stage for the essential features of the electronic structure we select YBCO as the target material. The unit cell of YBCO contains a bilayer of CuO_2 planes. The coupling between these two layers split the individual-layer derived bands. With respect to CDW formation it was demonstrated in earlier theoretical work⁴⁴ that the bilayer splitting determines primarily the relative orientation and phase of the CDWs in the two separate layers but does not have much effect on the structure of the CDW in the individual layers

themselves. In YBCO, the bilayer splitting even collapses in the near-nodal region at low doping⁴⁵. We therefore ascribe no vital role to the bilayer structure for the CDW itself and henceforth focus on a single copper–oxygen plane.

We start by modeling a single CuO₂ plane in YBCO including copper 4s and 3d_{x²-y²} as well as oxygen p_x and p_y orbitals. An effective three-band model is obtained in terms of the *d*- and *p*-orbitals by downfolding the original four-band model to refs. 7,46

$$H_{\text{kin}} = \sum_{\mathbf{k}, \sigma} \Psi_{\mathbf{k}, \sigma}^\dagger \begin{pmatrix} \varepsilon_d & 2t_{pd}s_x & -2t_{pd}s_y \\ 2t_{pd}s_x & \tilde{\varepsilon}_x(\mathbf{k}) & 4\tilde{t}_{pp}s_x s_y \\ -2t_{pd}s_y & 4\tilde{t}_{pp}s_x s_y & \tilde{\varepsilon}_y(\mathbf{k}) \end{pmatrix} \Psi_{\mathbf{k}, \sigma}, \quad (1)$$

with the three-spinor $\Psi_{\mathbf{k}, \sigma}^\dagger = (d_{\mathbf{k}, \sigma}^\dagger, p_{x\mathbf{k}, \sigma}^\dagger, p_{y\mathbf{k}, \sigma}^\dagger)$ and $s_{x,y} = \sin(k_{x,y}/2)$. ε_d denotes the onsite energy of the *d* orbital, t_{pd} and t_{ps} are the hopping amplitudes between *p*- and *d*- and *p*- and *s*-orbitals, respectively. In the downfolding procedure, the hopping processes via the copper 4s orbital renormalize the oxygen energies ε_p and generate indirect hopping $4t_{pp}^i$ between oxygen orbitals:

$$\tilde{\varepsilon}_{x,y} = \varepsilon_p + 4t_{pp}^i s_{x,y}^2; \quad \tilde{t}_{pp} = t_{pp}^i + t_{pp}^d; \quad t_{pp}^i = \frac{t_{ps}^2}{\varepsilon_F - \varepsilon_s}, \quad (2)$$

where ε_F is the Fermi energy and t_{pp}^d a small direct hopping amplitude. We adopt all the parameters entering Eqs. (1) and (2) from Andersen et al.⁴⁶, specifically $t_{pd} = 1.6$ eV, $\varepsilon_d - \varepsilon_p = 0.9$ eV, $t_{pp}^d = 0$ and $t_{pp}^i = -1.0$ eV. We diagonalize H_{kin} and focus only on the partially filled anti-bonding band; the irrelevant spin index is subsequently suppressed.

Bond-buckling phonon coupling. The out-of-plane B_{1g} vibrations of the oxygen atoms, as depicted in Fig. 1, naturally couple linearly to their local electric field E_z ⁴⁷. At this point, we neglect the motion of the almost four times heavier copper atoms. Consequently, we start from the ansatz

$$\mathcal{H}_{\text{ep}} = eE_z \sum_{\mathbf{n}} \left[\delta u_{x\mathbf{n}} p_{x\mathbf{n}}^\dagger p_{x\mathbf{n}} + \delta u_{y\mathbf{n}} p_{y\mathbf{n}}^\dagger p_{y\mathbf{n}} \right], \quad (3)$$

where $\delta u_{x,y\mathbf{n}}$ are the out-of-plane displacements of the oxygen atoms in unit cell \mathbf{n} . We project the *el-ph* Hamiltonian in Eq. (3), onto the anti-bonding band and obtain the effective Hamiltonian $\mathcal{H} = \mathcal{H}_{\text{el-ph}} + \mathcal{H}_{\text{ph}}$ with

$$\mathcal{H}_{\text{el-ph}} = \sum_{\mathbf{k}} \varepsilon_{\mathbf{k}} c_{\mathbf{k}}^\dagger c_{\mathbf{k}} + \sum_{\mathbf{q}, \mathbf{k}} g(\mathbf{q}; \mathbf{k}) c_{\mathbf{k}+\mathbf{q}}^\dagger c_{\mathbf{k}} (a_{\mathbf{q}} + a_{-\mathbf{q}}^\dagger), \quad (4)$$

where $c_{\mathbf{k}}^\dagger$ is the creation operator for the anti-bonding electrons with dispersion $\varepsilon_{\mathbf{k}}$, $a_{\mathbf{q}}$ annihilates a B_{1g} phonon mode, and $\mathcal{H}_{\text{ph}} = \hbar\Omega_p \sum_{\mathbf{q}} a_{\mathbf{q}}^\dagger a_{\mathbf{q}}$ (see Devereaux et al.⁴⁷ and Supplementary Notes 1 and 2). The momentum-dependent *el-ph* coupling is written $g(\mathbf{q}; \mathbf{k}) = \gamma \tilde{g}(\mathbf{q}; \mathbf{k})$ ⁴⁸, where γ is the coupling strength and

$$\tilde{g}(\mathbf{q}; \mathbf{k}) = \left[e_q^x \phi_x(\mathbf{k}') \phi_x(\mathbf{k}) + e_q^y \phi_y(\mathbf{k}') \phi_y(\mathbf{k}) \right], \quad (5)$$

with $\mathbf{k}' = \mathbf{k} + \mathbf{q}$. The eigenfunctions $\phi_{x,y}$ signify the orbital contents of the oxygen $p_{x,y}$ orbitals in the anti-bonding band. Similarly, the eigenvectors $e_q^{x,y}$ correspond to the normal mode of the out-of-plane displacements of the two oxygen atoms in the CuO₂ unit cell. The overall strength of the *el-ph* coupling is $\gamma = eE_z \sqrt{\hbar/2m\Omega_p}$, where m is the mass of the oxygen atom and $\Omega_p \sim 40$ meV is the frequency of the dispersionless B_{1g} mode. Adopting the electric-field value $eE_z = 3.56$ eV/Å from Johnston et al.⁴⁹ leads to $\gamma = 0.22$ eV. The eigenvectors for the B_{1g} mode are

$e_q^{x,y} = \mp \frac{\cos(q_{y,x}/2)}{M_{\mathbf{q}}}$ (see Supplementary Fig. 1), where the normalization factor $M_{\mathbf{q}} = \sqrt{\cos^2(q_x/2) + \cos^2(q_y/2)}$.

Earlier theoretical work^{33,50} on the B_{1g} phonon in optimally doped Bi-2212, argued that for an antinodal fermion state, $|g(\mathbf{q}; \mathbf{k})|^2$ is strongest for an axial scattering wavevector \mathbf{q} to the nearby antinodal final state. This value of \mathbf{q} is considerably smaller than \mathbf{q}_{CO} . Instead we find, when the Cu-4s orbital is properly included via the finite indirect hopping t_{pp}^i in Eq. (2), the anisotropic structure of $g(\mathbf{q}; \mathbf{k})$ changes qualitatively. The maximum of the coupling $|g(\mathbf{q}; \mathbf{k})|^2$ now occurs for larger axial wavevectors \mathbf{q}^* , that connect initial (\mathbf{k}_i^*) and final ($\mathbf{k}_i^* + \mathbf{q}^*$) Fermi surface states near the nodal points (see Fig. 2a, b). The resulting \mathbf{q}^* is quantitatively close to experimental values of \mathbf{q}_{CO} .

Fixing an initial state \mathbf{k}_i on the Fermi surface, we evaluate the maxima of $|g(\mathbf{q}; \mathbf{k}_i)|^2$ with respect to \mathbf{q} where $\mathbf{k}_i + \mathbf{q}$ is the final state on the Fermi surface, using the Nelder–Mead⁵¹ gradient approximation. We repeat this procedure as we vary the initial state \mathbf{k}_i along the Fermi surface branch in the first BZ quadrant and thereby identify the global maximum which we denote as $|g(\mathbf{q}^*; \mathbf{k}_i^*)|^2$. A plot of $|\tilde{g}(\mathbf{q}; \mathbf{k}_i^*)|^2$ vs. phonon wavevector \mathbf{q} is shown in Fig. 2a. The strongest scattering occurs at the axial \mathbf{q}^* indicated by the white arrow.

In order to determine what is special about \mathbf{k}_i^* and \mathbf{q}^* , we show the oxygen p_y -orbital resolved spectral function $A^y(\mathbf{k}, \varepsilon_F)$ in Fig. 2c. The highest spectral weight is obtained for $\mathbf{k} = \mathbf{k}_i^*$. In Fig. 2d, we parameterize the position on the Fermi surface by the angle $\psi_{\mathbf{k}} = \tan^{-1}(|k_y/k_x|)$. This panel indicates that it is the oxygen orbital content on the Fermi surface that determines \mathbf{k}_i^* and \mathbf{q}^* . The variation of the oxygen content is specifically controlled by the indirect hopping processes via the Cu-4s orbital.

Landau free energy and linked cluster expansion. We next calculate the doping evolution of \mathbf{q}^* and \mathbf{k}_i^* and collect the results in Fig. 3. The magnitude of \mathbf{q}^* comes close to the observed CDW ordering wavevector 0.3 (r.l.u.) and decreases with hole doping in a similar fashion as detected in X-ray experiments^{1,11,12,15,16,25}. It is therefore tempting to suspect a close connection. To pursue this idea, we return to the *el-ph* Hamiltonian Eq. (4) and assume a static mean-field lattice distortion

$$\sqrt{\frac{\hbar}{2m\Omega_p}} \langle a_{\mathbf{q}} + a_{-\mathbf{q}}^\dagger \rangle = \xi_{\mathbf{q}}, \quad (6)$$

with the four possible axial wavevectors $\pm\mathbf{q}^*$, $\pm\bar{\mathbf{q}}^*$ oriented either along the *x*- or the equivalent *y*-direction. We perform a linked-cluster expansion for the free energy to low orders in $\Delta_{\mathbf{q}} = eE_z \xi_{\mathbf{q}}$ (see Supplementary Note 3, Fig. 2 and Melikyan et al.^{52–54}):

$$\mathcal{F} = \mathcal{F}_0 + \sum_{\mathbf{q}=\mathbf{q}^*, \bar{\mathbf{q}}^*} \left[\frac{|\Delta_{\mathbf{q}}|^2}{4\gamma^2} (\hbar\Omega_p - 2\chi_{\mathbf{q}}^{(g)}) + |\Delta_{\mathbf{q}}|^4 \chi_{\mathbf{q}}^{(4)} \right] + |\Delta_{\mathbf{q}^*}|^2 |\Delta_{\bar{\mathbf{q}}^*}|^2 \chi_{\mathbf{q}^*, \bar{\mathbf{q}}^*}^{(4)}. \quad (7)$$

The static susceptibility $\chi_{\mathbf{q}}^{(g)}$ is defined as

$$\chi_{\mathbf{q}}^{(g)} = -2\gamma^2 \sum_{\mathbf{k}} |\tilde{g}(\mathbf{q}; \mathbf{k})|^2 \left[\frac{f(\varepsilon_{\mathbf{k}}) - f(\varepsilon_{\mathbf{k}+\mathbf{q}})}{\varepsilon_{\mathbf{k}} - \varepsilon_{\mathbf{k}+\mathbf{q}}} \right], \quad (8)$$

where $f(\varepsilon)$ denotes the Fermi distribution function. Upon cooling from high temperature, a lattice instability occurs at the \mathbf{q} value for which the coefficient $(\hbar\Omega_p - 2\chi_{\mathbf{q}}^{(g)})$ in the quadratic term first vanishes. This instability will necessarily produce an incommensurate charge modulation at the same \mathbf{q} . (In previous theoretical work, such a criterion was successfully employed to identify the correct CDW wavevectors for weakly correlated tellurides⁵³.)

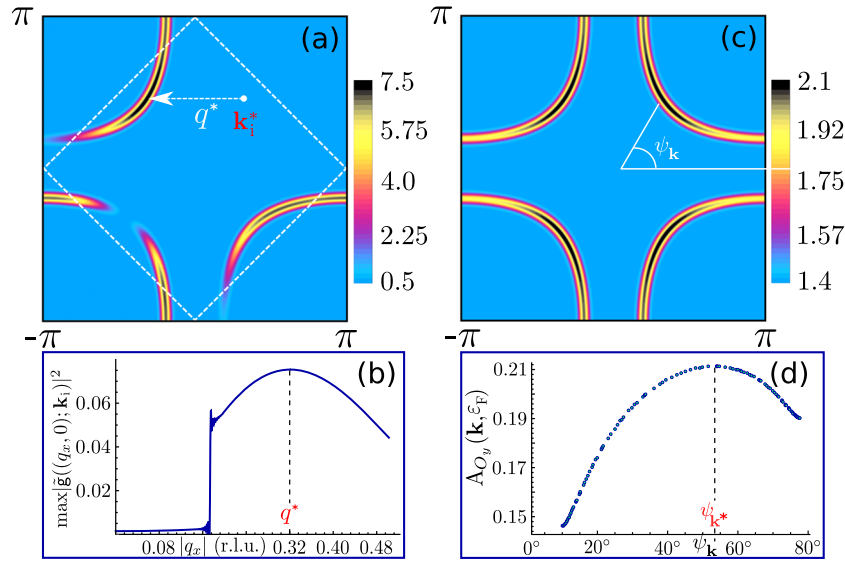


Fig. 2 Intrinsic features of electron-phonon (*el-ph*) coupling. **a** Plot of the dimensionless *el-ph* coupling $|\tilde{g}(\mathbf{q}; \mathbf{k}^*)|^2$ (in units of 10^{-2}) for phonon wavevectors \mathbf{q} that connect the initial \mathbf{k}_i^* and the scattered $\mathbf{k}_f^* + \mathbf{q}$ state, both on the Fermi surface at 10% hole doping. The strongest coupling occurs at the axial wavevector \mathbf{q}^* . **b** The maximum value of $|\tilde{g}(\mathbf{q}; \mathbf{k})|^2$ with respect to all initial momenta \mathbf{k}_i for axial wavevectors $\mathbf{q} = (q_x, 0)$. The global maximum is achieved at \mathbf{q}^* for the initial state at \mathbf{k}_i^* . **c** Spectral function $A_{O_y}(\mathbf{k}, \epsilon_F)$ (in units of 10^{-1}eV^{-1}) for the oxygen p_y -orbital electron on the Fermi surface. **d** The variation of $A_{O_y}(\mathbf{k}, \epsilon_F)$ along the Fermi surface parametrized by the angle $\psi_{\mathbf{k}}$ indicated in panel (**c**).

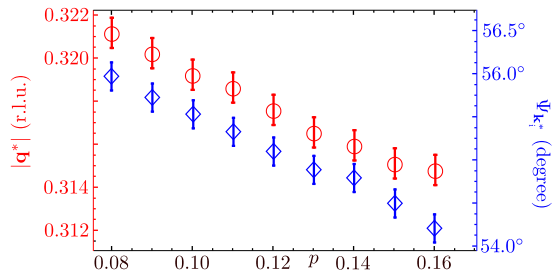


Fig. 3 Doping variation of phonon momentum. Hole doping (p) dependence of the axial wavevector \mathbf{q}^* (circles) and the angle $\psi_{\mathbf{k}_i^*}$ (diamonds) for the initial electronic momentum \mathbf{k}_i^* at which the global maximum of $|\tilde{g}(\mathbf{q}; \mathbf{k})|^2$ is achieved. The error bars represent the \mathbf{k} -space resolution.

Upon further cooling, the fourth-order coefficients decide between uniaxial and biaxial charge order. Because the magnitudes of the coefficients, and even the sign of $\chi_{\mathbf{q}^*}^{(4)}$, depend sensitively on specific parameter choices, it is difficult to make universal statements about the behavior of the quartic terms.

Returning to the quadratic term, we define for comparison the Lindhard function, $\chi_{\mathbf{q}}^{(L)}$, obtained by setting $\tilde{g}(\mathbf{q}; \mathbf{k}) = 1$ in Eq. (8); as shown in Fig. 4a, its weight is concentrated near the (π, π) point without any prominent wavevector related to nesting. Yet, as demonstrated in previous works^{29,30}, the momentum dependence of the *el-ph* coupling can by itself select the wavevector for a lattice instability and the concomitant charge order. Indeed, if the structure of $\tilde{g}(\mathbf{q}; \mathbf{k})$ is incorporated as in Eq. (8), the momentum-space weight of $\chi_{\mathbf{q}}^{(g)}$ redistributes (Fig. 4b). But, a clear instability wavevector still cannot be seen, and the largest values of $\chi_{\mathbf{q}}^{(g)}$ near the 2 meV are an order of magnitude smaller to meet the instability condition $2\chi_{\mathbf{q}}^{(g)} = \hbar\Omega_p = 40 \text{ meV}$. In particular, the axial wavevector \mathbf{q}^* for the global maximum of $|\tilde{g}(\mathbf{q}; \mathbf{k})|^2$ remains invisible.

The above analysis for the *el-ph* Hamiltonian Eq. (4) apparently fails to find an instability at the axial candidate wavevector \mathbf{q}^* . This naturally compromises the attempt to carry over a strategy, which so far has relied only on the electronic input parameters from density-functional theory (DFT), to strongly correlated cuprates. Seeking for the role the B_{1g} phonon in the CDW formation therefore requires to include quasiparticle renormalization effects beyond the DFT framework. Yet, including phonons in a multi-orbital model with strong electronic correlations is a demanding task. We therefore proceed with a trial ansatz to include correlation physics on a phenomenological level.

Phenomenological electronic correlation. The prevailing issue in the physics of underdoped cuprates is the conundrum of the pseudogap⁵⁵. The Fermi surface appears truncated to Fermi arcs centered around the BZ diagonals (the nodal regions) and it is obliterated near the BZ boundaries (the antinodal regions). In essence, well defined quasiparticles exist for near-nodal directions, while they are wiped out towards the antinodes. This motivates a simple ansatz for the Green function of the antibonding band quasiparticles, similar in spirit to Melikyan et al.⁵²

$$G(\mathbf{k}, \omega) = \frac{Z_{\mathbf{k}}}{\omega - \epsilon_{\mathbf{k}} + i\delta} + G_{\text{incoh}}, \quad (9a)$$

$$Z_{\mathbf{k}} = \begin{cases} \frac{1 - \cos(\psi_{\mathbf{k}} - \psi_{\text{max}})}{1 - \cos(45^\circ - \psi_{\text{max}})}; & \psi_{\mathbf{k}} \geq 45^\circ \\ \frac{1 - \cos(\psi_{\mathbf{k}} - \psi_{\text{min}})}{1 - \cos(45^\circ - \psi_{\text{min}})}; & \psi_{\mathbf{k}} < 45^\circ \end{cases}, \quad (9b)$$

for \mathbf{k} and $\psi_{\mathbf{k}}$ defined in the first quadrant of the BZ (see Fig. 2c). $Z_{\mathbf{k}}$ is the quasiparticle weight tailored to continuously decrease from 1 at the nodal point to zero at the BZ faces (see Supplementary Fig. 3 for a pictorial illustration of $Z_{\mathbf{k}}$). $\psi_{\text{max/min}}$ denotes the largest/smallest angle $\psi_{\mathbf{k}}$ for the Fermi surface momenta (k_F, π) and (π, k_F) , respectively. The \mathbf{k} -dependence in Eq. (9b) is analogously carried over to the other segments of the Fermi

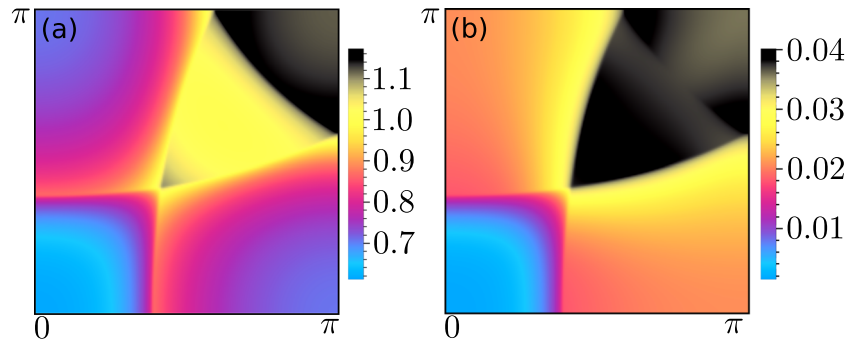


Fig. 4 Momentum space structure of free susceptibility. **a** Lindhard function $\chi_{\mathbf{q}}^{(L)}/\gamma^2$ and **b** $\chi_{\mathbf{q}}^{(9)}/\gamma^2$ (in units of $(\text{eV})^{-1}$) in the first quadrant of the Brillouin zone at 110 K and 10% hole doping. Color scheme—the absolute values with the minimum (blue) and the maximum (black).

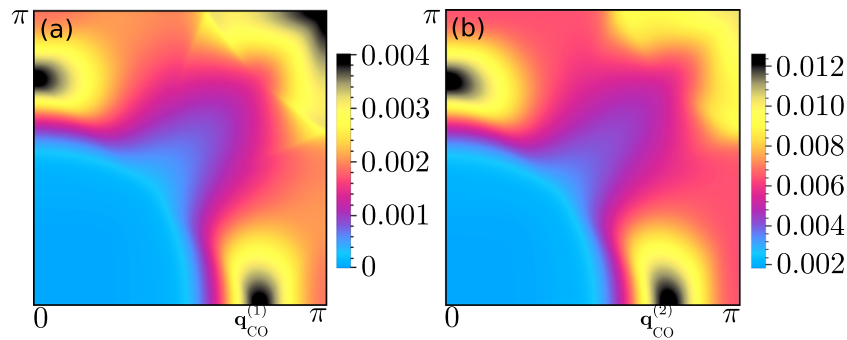


Fig. 5 Momentum space structure of renormalized susceptibility. **a** Renormalized static susceptibility $\chi_{\mathbf{q}}^{(gZ)}/\gamma^2$ and **b** $\chi_{\mathbf{q}}^{(gZ)}/\gamma^2$ (in units of $(\text{eV})^{-1}$) modified further by a renormalized dispersion in the square brackets of Eq. (10), in the first quadrant of the Brillouin zone at 110 K and 10% hole doping. Color scheme—the absolute values with the minimum (blue) and the maximum (black).

surfaces. We emphasize that Eq. (9b) is an ad hoc, phenomenological ansatz. The desired quantitative information—in particular with sufficient momentum-space resolution—for the anisotropic quasiparticle-weight renormalization at different doping levels is not available. The latter is a hard task by itself for strongly correlated electron theory.

The ansatz in Eqs. (9a) and (9b) leads to the renormalized static susceptibility

$$\chi_{\mathbf{q}}^{(gZ)} \approx -2\gamma^2 \sum_{\mathbf{k}} Z_{\mathbf{k}} Z_{\mathbf{k}+\mathbf{q}} |\tilde{g}(\mathbf{q}; \mathbf{k})|^2 \left[\frac{f(\epsilon_{\mathbf{k}}) - f(\epsilon_{\mathbf{k}+\mathbf{q}})}{\epsilon_{\mathbf{k}} - \epsilon_{\mathbf{k}+\mathbf{q}}} \right], \quad (10)$$

where the contributions from the incoherent part of $G(\mathbf{k}, \omega)$ are neglected (see Supplementary Note 4).

We examine the impact of the quasiparticle weight factors on the susceptibility $\chi_{\mathbf{q}}^{(gZ)}$ in Fig. 5a. The highly anisotropic variation of $Z_{\mathbf{k}}$ reduces the susceptibility around the BZ diagonal and creates new structures along the axes including the global maximum at axial wavevectors $\mathbf{q}_{\text{CO}}^{(1)}$ and $\bar{\mathbf{q}}_{\text{CO}}^{(1)}$, which are larger than, but close to, \mathbf{q}^* or $\bar{\mathbf{q}}^*$ for which the $el-ph$ coupling is strongest.

In a second step we incorporate—besides the anisotropic weight factors $Z_{\mathbf{k}}$ —also the correlation induced renormalization of the band dispersion by replacing $\epsilon_{\mathbf{k}} \Rightarrow \epsilon_{\mathbf{k}}^{\text{R}}$ in Eq. (9a) and hence also in the square bracket of Eq. (10). For this purpose, we adopt a phenomenological fit to the measured ARPES dispersion applied previously to data for optimally doped Bi-2212⁵⁶. Compared to the bare dispersion, $\epsilon_{\mathbf{k}}^{\text{R}}$ has an almost three times narrower bandwidth and the nodal Fermi velocity v_{F} is similarly reduced, while the shape of the Fermi surface remains almost preserved. The susceptibility $\chi_{\mathbf{q}}^{(gZ)}$ with the renormalized $\epsilon_{\mathbf{k}}^{\text{R}}$ is shown in

Fig. 5b. We observe that the axial peaks are retained at wavevectors $\mathbf{q}_{\text{CO}}^{(2)}$ with $q^* < q_{\text{CO}}^{(2)} < q_{\text{CO}}^{(1)}$, whereas the peak at the (π, π) point loses its strength. $q_{\text{CO}}^{(2)}$ is about 16% larger than q^* and follows the same doping dependence as q^* . Furthermore, the strength of the peak at $\mathbf{q}_{\text{CO}}^{(2)}$ has tripled. This increase is naturally tied to the downward renormalization of v_{F} . So, we conclude that it apparently requires both a correlation-induced quasiparticle renormalization, and a specific momentum dependence of the $el-ph$ coupling to generate the axial and incommensurate candidate wavevector $\mathbf{q}_{\text{CO}}^{(2)}$ for the anticipated lattice and concomitant CDW instability.

In reaching our conclusion, we have manifestly neglected the life-time broadening effects on the nodal quasiparticles; material difference matter. While the majority of ARPES experiments, based on Bi-based cuprates⁵⁷, report a quantitatively larger quasiparticle broadening (~ 10 meV near the gap node⁵⁸), state-of-the-art transport experiments provide much smaller broadening in YBCO. Notably, microwave measurements in $\text{YBa}_2\text{Cu}_3\text{O}_{6.5}$ find transport scattering rates of order 0.1 meV⁵⁹, which is 100 times smaller than typical values quoted for Bi-2212, which is most likely connected to the inhomogeneity of the samples. Indeed, STM experiments^{60,61} show that Bi based cuprates (Bi-2201 and Bi-2212) host a relatively large material inhomogeneity, while YBCO is believed to be homogeneous. It seems to us likely that scattering rates obtained from ARPES in Bi-2212 include significant disorder broadening at low temperature and energy, and are not relevant to YBCO.

Numerical estimate of B_{1g} phonon softening. Without aiming at a quantitative description we nevertheless translate the obtained

result into an estimate. The absolute units in Fig. 5b indicate that $\chi_{\mathbf{q}_{\text{CO}}^{(2)}}^{(gZ)} \ll \hbar\Omega_p$, and we are therefore far from meeting the mean-field instability criterion. Nonetheless, the *el-ph* coupling inevitably also alters the frequency of the participating phonons. Based on Grüner et al.⁶², the renormalized B_{1g} phonon frequency $\tilde{\omega}_{\mathbf{q}}$ follows from

$$\tilde{\omega}_{\mathbf{q}}^2 = \Omega_p^2(1 - \lambda_{\mathbf{q}}), \quad \lambda_{\mathbf{q}} = \frac{2\chi_{\mathbf{q},\Omega_p}^{(gZ)}}{\hbar\Omega_p}, \quad (11)$$

where $\chi_{\mathbf{q},\Omega_p}^{(gZ)}$ is the real part of the susceptibility at the bare phonon frequency Ω_p . At 110 K and $\mathbf{q} = \mathbf{q}_{\text{CO}}^{(2)}$, the dynamical susceptibility is slightly smaller than its static zero-frequency value, from which Eq. (11) gives $\tilde{\omega}_{\mathbf{q}} \simeq 0.987\Omega_p$, i.e., a softening of 1.3%. Upon cooling $\chi_{\mathbf{q},\Omega_p}^{(gZ)}$ increases slightly and the softening reaches $\sim 1.5\%$ at around 3 K. For reference we mention that in Raichle et al.²⁶, the measured softening of the B_{1g} phonon frequency in $\text{YBa}_2\text{Cu}_3\text{O}_7$ was about 6% at 3 K for $\mathbf{q} \sim (0, 0.3)$.

Several factors may act to enhance the *el-ph* coupling in underdoped cuprates. We recall that a dispersion $\epsilon_{\mathbf{k}}^R$ for an optimally doped material was used for the evaluation of $\chi_{\mathbf{q}}^{(gZ)}$. On the underdoped side, the nodal Fermi velocity in Bi-2212 drops by as much as 50%⁶³. Such a drop necessarily enhances $\chi_{\mathbf{q}_{\text{CO}}^{(2)}}^{(gZ)}$ and the corresponding phonon softening is estimated to rise to about 2.12% reflecting somewhat enhanced CDW correlations at wavevectors $\mathbf{q}_{\text{CO}}^{(2)}$ for underdoped materials. Furthermore, strong correlations in the underdoped cuprates decrease the copper and increase the oxygen orbital content on the Fermi surface, thereby enlarging the susceptibility at $\mathbf{q}_{\text{CO}}^{(2)}$. One may argue that a considerably larger charge susceptibility—as an outcome of our calculation—would strengthen the case for the proposed mechanism. Yet, any theory for the CDW in Y- or Bi-based cuprates has to be reconciled with the prevailing fact that ARPES experiments fail to identify signatures of spectral changes or electronic reconstruction in the charge ordered phase. Even, in charge-stripe ordered Nd-doped LSCO, the interpretation of line-shape changes remains subtle^{64,65}. For these reasons, the anticipated CDW can be considered weak.

The rough estimates presented above for an only weak phonon-based tendency towards charge order is—in this sense—not contradicting, but it is clearly too weak to generate a long range ordered CDW state. Still, the charge order in underdoped cuprates is in fact short ranged with moderate planar correlation lengths^{14–16}, and is most likely nucleated by defects^{10,31,66}. A strong magnetic field^{67,68} or uniaxial pressure²⁷ is needed to enhance the planar correlation length and to even achieve 3D CDW order. The magnetic field suppresses superconductivity, which otherwise stops the charge correlations from growing upon cooling.

Discussion

Our proposed mechanism therefore appears compatible with experimental observations. The momentum-dependence of the *el-ph* coupling to the B_{1g} bond-buckling phonon and the specific variation of the oxygen orbital content on the Fermi surface select an incommensurate, axial wavevector \mathbf{q}^* for which the lattice is most susceptible to deform. But only in conjunction with the strong and anisotropic renormalization of the correlated electrons in the copper oxygen planes does the corresponding susceptibility develop the required enhancement near \mathbf{q}^* to move the *el-ph* systems at least towards a charge ordered state with an axial wavevector $\mathbf{q}_{\text{CO}}^{(2)}$ near \mathbf{q}^* .

Compared to bilayer materials like YBCO the case of single-layer cuprates is more complicated. In pristine Hg-1201 and Bi-2201, the CuO_2 planes have mirror symmetries that prohibit a linear coupling between the B_{1g} phonon and the electrons. However, both of these materials are doped by large concentrations of interstitial oxygen atoms that reside above the CuO_2 plane. These unscreened dopants are the source of large electric fields in the CuO_2 plane and act as nucleation sites for CDW patches⁶⁹. In bilayer cuprates viz. Bi-2212, such interstitial oxygen atoms generate an electric field of the order of few eV/Å which in turn strongly amplifies (up to a factor of 5) the strength of the B_{1g} *el-ph* coupling⁷⁰. These field strengths are comparable to that obtained for YBCO, and must (by symmetry) produce a linear coupling between the B_{1g} phonon and the CDW. Based on these empirical facts, we expect a similar strong enhancement of the B_{1g} coupling in the single-layer cuprates, such as Bi-2201 and Hg-1201.

An important question is the extent to which such inhomogeneous *el-ph* coupling is visible in the phonon dispersion. Provided the phonons are harmonic, the lattice distortion associated with the local electric fields should not shift the phonon frequencies; rather, the *el-ph* matrix element will be distributed across a range of values leading to a broadening of the phonon dispersion near the ordering wavevector. However, the scale of the broadening, and in particular, how it compares with other sources of apparent broadening, as discussed in Ahmadova et al.⁴², remains unsettled.

A determination of boundaries for the CDW phase in the temperature vs. doping phase diagram is beyond the scope of our current work, but we offer arguments for the relevant ingredients which determine the variation with respect to hole doping. The magnitude of the charge susceptibility at the anticipated ordering wavevector is controlled by (i) the magnitude of the *el-ph* coupling for initial and scattered electron momenta on the Fermi surface, (ii) the nodal Fermi velocity, and (iii) the quasiparticle weight at those Fermi surface points where $g(\mathbf{q}; \mathbf{k})$ achieves its largest values in the near nodal regions.

First, the global maximum value of $g(\mathbf{q}; \mathbf{k})$ on the doping dependent Fermi surfaces drops with hole doping, i.e. upon leaving the underdoped region toward the overdoped side (see Supplementary Note 5, Fig. 4). Simultaneously, the nodal Fermi velocity almost doubles⁶³. Both of these trends reduce the charge susceptibility.

The ansatz for the quasiparticle weight along the Fermi surface reflects the Fermi arc formation in underdoped cuprates; the quasiparticles are assumed intact in the near-nodal region with only a weak quasiparticle weight reduction. Necessarily we have to expect that the quasiparticle-weight—even in the near-nodal regions—will shrink upon lowering the hole doping concentration towards the insulator. Taken together, these trends naturally suggest a dome shaped CDW region in the temperature vs. doping phase diagram centered around an underdoped composition. This qualitative reasoning complies with the experimental findings.

For the intra-unit cell symmetry of the charge redistribution in the CDW state, our proposed scenario leads to a predominant *s*-symmetry form factor. Since, Cu-*d*-orbital character is admixed to the near-nodal Fermi surface points connected by \mathbf{q}^* , also the charge on the Cu ion will be sizably modulated, as indeed is detected by nuclear magnetic resonance⁸. Although a prominent *d*-wave character for the charge modulations on the oxygen *p*-orbitals has been reported in early resonant X-ray scattering⁷¹ and STM experiments⁷², this initial conclusion has recently been disputed. Instead, the X-ray data in McMahon et al.⁷³ rather support a dominant *s*-wave form factor and are therefore compatible with the prediction from the phonon scenario.

At the core of our proposal is that it requires both, correlated electron physics and the coupling to the lattice degrees of freedom to address the CDW in cuprates. The special momentum–space structure of the el - ph coupling matrix element for the B_{1g} bond-buckling phonon has revealed an important ingredient which was not appreciated in electronic theories before. This is the variation of the oxygen orbital content on the Fermi surface, which dictates for which momenta the coupling, here to the B_{1g} phonon, is strongest. This may prove as a relevant step forward to elucidate the true complexity of the CDW phenomenon in cuprates. Strong electronic interactions by themselves develop charge correlations, but we infer that these may lock into an incommensurate charge-ordering pattern in Y- and Bi-based cuprates only in conjunction with a specific momentum-dependent microscopic coupling to the lattice.

Data availability

The data sets generated and analysed during the current study are available from the corresponding author upon reasonable request.

Received: 12 February 2020; Accepted: 18 August 2020;

Published online: 18 September 2020

References

- Comin, R. & Damascelli, A. Resonant X-ray scattering studies of charge order in cuprates. *Annu. Rev. Condens. Matter Phys.* **7**, 369 (2016).
- Caprara, S., DiCastro, C., Seibold, G. & Grilli, M. Dynamical charge density waves rule the phase diagram of cuprates. *Phys. Rev. B* **95**, 224511 (2017).
- Verret, S., Charlebois, M., Sénéchal, D. & Tremblay, A. M. S. Subgap structures and pseudogap in cuprate superconductors: role of density waves. *Phys. Rev. B* **95**, 054518 (2017).
- Chatterjee, S. & Sachdev, S. Fractionalized Fermi liquid with bosonic chargons as a candidate for the pseudogap metal. *Phys. Rev. B* **94**, 205117 (2016).
- Efetov, K. B., Meier, H. & Pépin, C. Pseudogap state near a quantum critical point. *Nat. Phys.* **9**, 442 (2013).
- Tselik, A. M. & Chubukov, A. V. Composite charge order in the pseudogap region of the cuprates. *Phys. Rev. B* **89**, 184515 (2014).
- Atkinson, W. A., Kampf, A. P. & Bulut, S. Charge order in the pseudogap phase of cuprate superconductors. *N. J. Phys.* **17**, 013025 (2015).
- Wu, T. et al. Magnetic-field-induced charge-stripe order in the high-temperature superconductor $\text{YBa}_2\text{Cu}_3\text{O}_y$. *Nature* **477**, 191 (2011).
- Wu, T. et al. Emergence of charge order from the vortex state of a high-temperature superconductor. *Nat. Commun.* **4**, 2113 (2013).
- Wu, T. et al. Incipient charge order observed by NMR in the normal state of $\text{YBa}_2\text{Cu}_3\text{O}_y$. *Nature* **6**, 6438 (2015).
- Comin, R. et al. Charge order driven by fermi-arc instability in $\text{Bi}_2\text{Sr}_{2-x}\text{La}_x\text{CuO}_{6+\delta}$. *Science* **343**, 390 (2014).
- daSilvaNeto, E. H. et al. Ubiquitous interplay between charge ordering and high-temperature superconductivity in cuprates. *Science* **343**, 393 (2014).
- Kohsaka, Y. et al. An intrinsic bond-centered electronic glass with unidirectional domains in underdoped cuprates. *Science* **315**, 1380 (2007).
- Ghiringhelli, G. et al. Long-range incommensurate charge fluctuations in $(\text{Y,Nd})\text{Ba}_2\text{Cu}_3\text{O}_{6+x}$. *Science* **337**, 821 (2012).
- Chang, J. et al. Direct observation of competition between superconductivity and charge density wave order in $\text{YBa}_2\text{Cu}_3\text{O}_{6.67}$. *Nat. Phys.* **8**, 871 (2012).
- Blackburn, E. et al. X-ray diffraction observations of a charge-density-wave order in superconducting ortho-II $\text{YBa}_2\text{Cu}_3\text{O}_{6.54}$ single crystals in zero magnetic field. *Phys. Rev. Lett.* **110**, 137004 (2013).
- Peng, Y. Y. et al. Direct observation of charge order in underdoped and optimally doped $\text{Bi}_2(\text{Sr,Ln})_2\text{CuO}_{6,\delta}$ by resonant inelastic x-ray scattering. *Phys. Rev. B* **94**, 184511 (2016).
- Hücker, M. et al. Stripe order in superconducting $\text{La}_{2-x}\text{Ba}_x\text{CuO}_4$ ($0.095 \leq x \leq 0.155$). *Phys. Rev. B* **83**, 104506 (2011).
- Corboz, P., Rice, T. M. & Troyer, M. Competing States in the t - J model: uniform d -wave state versus stripe state. *Phys. Rev. Lett.* **113**, 046402 (2014).
- Zheng, B.-X. et al. Stripe order in the underdoped region of the two-dimensional Hubbard model. *Science* **358**, 1155 (2017).
- Jiang, H.-C. & Devereaux, T. P. Superconductivity in the doped Hubbard model and its interplay with next-nearest hopping t . *Science* **365**, 1424 (2019).
- Huang, E. W. et al. Numerical evidence of fluctuating stripes in the normal state of high- T_c cuprate superconductors. *Science* **358**, 1161 (2017).
- Sau, J. D. & Sachdev, S. Mean-field theory of competing orders in metals with antiferromagnetic exchange interactions. *Phys. Rev. B* **89**, 075129 (2014).
- Bulut, S., Atkinson, W. A. & Kampf, A. P. Spatially modulated electronic nematicity in the three-band model of cuprate superconductors. *Phys. Rev. B* **88**, 155132 (2013).
- Peng, Y. Y. et al. Re-entrant charge order in overdoped $(\text{Bi,Pb})_{2+12}\text{Sr}_{1+88}\text{CuO}_{6+d}$ outside the pseudogap regime. *Nat. Mater.* **17**, 697 (2018).
- Raichle, M. et al. Highly anisotropic anomaly in the dispersion of the copper-oxygen bond-bending phonon in superconducting $\text{YBa}_2\text{Cu}_3\text{O}_7$ from inelastic neutron scattering. *Phys. Rev. Lett.* **107**, 177004 (2011).
- Kim, H. H. et al. Uniaxial pressure control of competing orders in a high-temperature superconductor. *Science* **362**, 1040 (2018).
- LeTacon, M. et al. Inelastic X-ray scattering in $\text{YBa}_2\text{Cu}_3\text{O}_{6.6}$ reveals giant phonon anomalies and elastic central peak due to charge-density-wave formation. *Nat. Phys.* **10**, 52 (2013).
- Eiter, H.-M. et al. Alternative route to charge density wave formation in multiband systems. *Proc. Natl Acad. Sci. USA* **110**, 64 (2013).
- Johannes, M. D. & Mazin, I. I. Fermi surface nesting and the origin of charge density waves in metals. *Phys. Rev. B* **77**, 165135 (2008).
- Campi, G. et al. Inhomogeneity of charge-density-wave order and quenched disorder in a high- T_c superconductor. *Nature* **525**, 359 (2015).
- Forgan, E. M. et al. The microscopic structure of charge density waves in underdoped $\text{YBa}_2\text{Cu}_3\text{O}_{6.54}$ revealed by X-ray diffraction. *Nat. Commun.* **6**, 10064 (2015).
- Cuk, T. et al. Coupling of the B_{1g} phonon to the antinodal electronic states of $\text{Bi}_2\text{Sr}_2\text{Ca}_{0.92}\text{Y}_{0.08}\text{Cu}_2\text{O}_{8+\delta}$. *Phys. Rev. Lett.* **93**, 117003 (2004).
- Chung, J.-H. et al. In-plane anisotropy and temperature dependence of oxygen phonon modes in $\text{YBa}_2\text{Cu}_3\text{O}_{6.95}$. *Phys. Rev. B* **67**, 014517 (2003).
- Reznik, D. et al. Temperature dependence of the bond-stretching phonon anomaly in $\text{YBa}_2\text{Cu}_3\text{O}_{6.95}$. *Phys. Rev. B* **78**, 094507 (2008).
- Pintschovius, L. et al. Oxygen phonon branches in $\text{YBa}_2\text{Cu}_3\text{O}_7$. *Phys. Rev. B* **69**, 214506 (2004).
- Uchiyama, H. et al. Softening of Cu-O bond stretching phonons in tetragonal $\text{HgBa}_2\text{CuO}_{4+\delta}$. *Phys. Rev. Lett.* **92**, 197005 (2004).
- Astuto, M., Mirone, A., Giura, P., Colson, D. & Forget, A. et al. Softening of Cu-O bond stretching phonons in tetragonal $\text{HgBa}_2\text{CuO}_{4+\delta}$. *J. Phys.* **15**, 8827 (2003).
- Tejssner, T. et al. Anomalous dispersion of longitudinal optical phonons in oxygen-doped $\text{La}_{2-x}\text{Sr}_x\text{CuO}_{4+\delta}$. *Phys. Rev. B* **101**, 100504 (2020).
- Park, S. R. et al. Evidence for a charge collective mode associated with superconductivity in copper oxides from neutron and x-ray scattering measurements of $\text{La}_{2-x}\text{Sr}_x\text{CuO}_4$. *Phys. Rev. B* **89**, 020506 (2014).
- Graf, J. et al. Bond stretching phonon softening and kinks in the angle-resolved photoemission spectra of optimally doped $\text{Bi}_2\text{Sr}_{1.6}\text{La}_{0.4}\text{Cu}_2\text{O}_{6+\delta}$ superconductors. *Phys. Rev. Lett.* **100**, 227002 (2008).
- Ahmadova, I., Sterling, T. C., Sokolik, A. C., Abernathy, D. L. & Greven, M. et al. Phonon spectrum of underdoped $\text{HgBa}_2\text{CuO}_{4+\delta}$ investigated by neutron scattering. *Phys. Rev. B* **101**, 184508 (2020).
- Li, J. et al. Multiorbital charge-density-wave excitations and concomitant phonon anomalies in $\text{Bi}_2\text{Sr}_2\text{LaCuO}_{6+}$. *Proc. Natl Acad. Sci. USA* **117**, 16219 (2020).
- Maharaj, A. V., Hosur, P. & Raghu, S. Crisscrossed stripe order from interlayer tunneling in hole-doped cuprates. *Phys. Rev. B* **90**, 125108 (2014).
- Fournier, D. et al. Loss of nodal quasiparticle integrity in underdoped $\text{YBa}_2\text{Cu}_3\text{O}_{6+x}$. *Nat. Phys.* **6**, 905 (2010).
- Andersen, O. K., Liechtenstein, A. I., Jepsen, O. & Paulsen, F. LDA energy bands, low-energy hamiltonians, t' , t'' , $t_1(\mathbf{k})$ and J_{\perp} . *J. Phys. Chem. Solids* **56**, 1573 (1995).
- Devereaux, T. P., Virosztek, A. & Zawadowski, A. Charge-transfer fluctuation, d -wave superconductivity, and the B_{1g} Raman phonon in cuprates. *Phys. Rev. B* **51**, 505 (1995).
- Devereaux, T. P., Virosztek, A. & Zawadowski, A. Neutron scattering and the B_{1g} phonon in the cuprates. *Phys. Rev. B* **59**, 14168 (1999).
- Johnston, S. et al. Systematic study of electron-phonon coupling to oxygen modes across the cuprates. *Phys. Rev. B* **82**, 064513 (2010).
- Devereaux, T. P., Cuk, T., Shen, Z. X. & Nagaosa, N. Anisotropic electron-phonon interaction in the cuprates. *Phys. Rev. Lett.* **93**, 117004 (2004).
- Lagarias, J., Reeds, J., Wright, M. & Wright, P. Convergence properties of the nelder-mead simplex method in low dimensions. *SIAM J. Optimiz.* **9**, 112 (1998).
- Melikyan, A. & Norman, M. R. Symmetry of the charge density wave in cuprates. *Phys. Rev. B* **89**, 024507 (2014).
- Yao, H., Robertson, J. A., Kim, E.-A. & Kivelson, S. A. Theory of stripes in quasi-two-dimensional rare-earth tellurides. *Phys. Rev. B* **74**, 245126 (2006).
- Mahan, G. D. *Condensed Matter in a Nutshell*. (Princeton, Princeton University Press, 2011).
- Lee, P. A., Nagaosa, N. & Wen, X.-G. Doping a Mott insulator: physics of high-temperature superconductivity. *Rev. Mod. Phys.* **78**, 17 (2006).

56. Norman, M. R. Linear response theory and the universal nature of the magnetic excitation spectrum of the cuprates. *Phys. Rev. B* **75**, 184514 (2007).
57. Li, H. et al. Coherent organization of electronic correlations as a mechanism to enhance and stabilize high- T_c cuprate superconductivity. *Nat. Commun.* **9**, 26 (2018).
58. Yamasaki, T. et al. Unmasking the nodal quasiparticle dynamics in cuprate superconductors using low-energy photoemission. *Phys. Rev. B* **75**, 140513 (2007).
59. Harris, R. et al. Phenomenology of a-axis and b-axis charge dynamics from microwave spectroscopy of highly ordered $\text{YBa}_2\text{Cu}_3\text{O}_{6.50}$ and $\text{YBa}_2\text{Cu}_3\text{O}_{6.993}$. *Phys. Rev. B* **74**, 104508 (2006).
60. Pan, S. H. et al. Microscopic electronic inhomogeneity in the high- T_c superconductor $\text{Bi}_2\text{Sr}_2\text{CaCu}_2\text{O}_{8+x}$. *Nature* **413**, 282 (2001).
61. Fischer, Ø., Kugler, M., Maggio-Aprile, I., Berthod, C. & Renner, C. Scanning tunneling spectroscopy of high-temperature superconductors. *Rev. Mod. Phys.* **79**, 353 (2007).
62. Grüner, G. *Density Waves in Solids* (Westview Press, 2009).
63. Vishik, I. M. et al. Doping-dependent nodal fermi velocity of the high-temperature superconductor $\text{Bi}_2\text{Sr}_2\text{CaCu}_2\text{O}_{8+\delta}$ revealed using high-resolution angle-resolved photoemission spectroscopy. *Phys. Rev. Lett.* **104**, 207002 (2010).
64. Matt, C. E. et al. Electron scattering, charge order, and pseudogap physics in $\text{La}_{1.6-x}\text{Nd}_{0.4}\text{Sr}_x\text{CuO}_4$: an angle-resolved photoemission spectroscopy study. *Phys. Rev. B* **92**, 134524 (2015).
65. Kivelson, S. A. & Lederer, S. Linking the pseudogap in the cuprates with local symmetry breaking: a commentary. *Proc. Natl Acad. Sci. USA* **116**, 14395 (2019).
66. Atkinson, W. A., Ufkes, S. & Kampf, A. P. Structure of the charge density wave in cuprate superconductors: Lessons from NMR. *Phys. Rev. B* **97**, 125147 (2018).
67. Gerber, S. et al. Three-dimensional charge density wave order in $\text{YBa}_2\text{Cu}_3\text{O}_{6.67}$ at high magnetic fields. *Science* **350**, 949 (2015).
68. Jang, H. et al. Ideal charge-density-wave order in the high-field state of superconducting YBCO. *Proc. Natl Acad. Sci. USA* **113**, 14645 (2016).
69. Tabis, W. et al. Synchrotron x-ray scattering study of charge-density-wave order in $\text{HgBa}_2\text{CuO}_{4+\delta}$. *Phys. Rev. B* **96**, 134510 (2017).
70. Johnston, S., Vernay, F. & Devereaux, T. P. Impact of an oxygen dopant in $\text{Bi}_2\text{Sr}_2\text{CaCu}_2\text{O}_{8+\delta}$. *EPL* **86**, 37007 (2009).
71. Comin, R. et al. Symmetry of charge order in cuprates. *Nat. Mater.* **14**, 796 (2015).
72. Fujita, K. et al. Direct phase-sensitive identification of a d-form factor density wave in underdoped cuprates. *Proc. Natl Acad. Sci. USA* **111**, E3026 (2014).
73. McMahon, C. et al. Orbital symmetries of charge density wave order in $\text{YBa}_2\text{Cu}_3\text{O}_{6+x}$. Preprint at: <https://arxiv.org/abs/1904.12929> (2019).

Acknowledgements

We acknowledge helpful conversations with T.P. Devereaux, P.J. Hirschfeld, T. Kopp, L. Chioncel, S. Johnston, and C. Morice. W.A.A. acknowledges support by the Natural Sciences and Engineering Research Council (NSERC) of Canada. A.P.K. acknowledges support by the Deutsche Forschungsgemeinschaft (DFG, German Research Foundation)-project-ID-107745057-TRR 80. Open access funding provided by Projekt DEAL.

Author contributions

S.B. carried out the analytical work. A.P.K. conceived the project. All authors (S.B., A.P.K., and W.A.A.) discussed the results and the implications and contributed to the paper at all stages.

Competing interests

The authors declare no competing interests.

Additional information

Supplementary information is available for this paper at <https://doi.org/10.1038/s42005-020-00430-1>.

Correspondence and requests for materials should be addressed to S.B.

Reprints and permission information is available at <http://www.nature.com/reprints>

Publisher's note Springer Nature remains neutral with regard to jurisdictional claims in published maps and institutional affiliations.



Open Access This article is licensed under a Creative Commons Attribution 4.0 International License, which permits use, sharing, adaptation, distribution and reproduction in any medium or format, as long as you give appropriate credit to the original author(s) and the source, provide a link to the Creative Commons license, and indicate if changes were made. The images or other third party material in this article are included in the article's Creative Commons license, unless indicated otherwise in a credit line to the material. If material is not included in the article's Creative Commons license and your intended use is not permitted by statutory regulation or exceeds the permitted use, you will need to obtain permission directly from the copyright holder. To view a copy of this license, visit <http://creativecommons.org/licenses/by/4.0/>.

© The Author(s) 2020